Physics and Chemistry of Minerals (2022) 49:23
https://doi.org/10.1007/s00269-022-01195-5

ORIGINAL PAPER

# Thermodynamic properties of geikielite ($MgTiO_3$) and ilmenite ($FeTiO_3$) derived from vibrational methods combined with Raman and infrared spectroscopic data

Michael H. G. Jacobs[1] · Arie P. van den Berg[2,3] · Rainer Schmid-Fetzer[1] · Jellie de Vries[4] · Wim van Westrenen[3] · Yue Zhao[3]

Received: 1 February 2022 / Accepted: 21 April 2022 / Published online: 9 June 2022


## Abstract

We present a model for the lattice vibrational density of states of $MgTiO_3$ (geikielite) and $FeTiO_3$ (ilmenite) that predicts thermodynamic properties, in agreement with observational data. The model is based on Kieffer's method combined with spectroscopic data. For both substances experimental data sets are influenced by non-stoichiometry. For geikielite that affects the volume, whereas for ilmenite volume and bulk modulus are affected. We show that Kieffer's method enables predicting bulk moduli in pressure–temperature space. We demonstrate that intrinsic anharmonicity or electronic effects significantly affect the heat capacity of ilmenite, whereas that is not the case for geikielite. We use Kieffer's method to derive multiple-Einstein models, from which we demonstrate that thermodynamic properties are insignificantly influenced by dispersion in Grüneisen, mode-q and anharmonicity parameters for both substances. We show that our results enable predicting thermodynamic properties and shear modulus of the solid solution formed from geikielite and ilmenite. Geikielite and ilmenite are added to our thermodynamic database for the system MgO–$SiO_2$–FeO, to enable modeling phase stability and physical properties of titanium-rich reservoirs in the Earth's Moon.

**Keywords** Vibrational density of states · Anharmonicity · Elasticity · Geikielite · Ilmenite

## Introduction

The geikielite–ilmenite solid solution is the main titanium ore on Earth, and a mineral of key importance in models for the chemical and thermal evolution of the interior of Earth's Moon. Dynamical and geochemical models of Moon formation indicate that the Moon was covered by a deep magma ocean, shortly after its formation (e.g., Lock et al. 2018; Nakajima and Stevenson 2018; Steenstra et al. 2016, 2020). Experimental studies of the progressive solidification of this magma ocean indicate that Fe-rich geikielite–ilmenite crystals form late in the ocean's crystallization sequence in the shallow subsurface of the Moon, underneath the growing plagioclase-rich crust (Lin et al. 2017a, b, 2020; Charlier et al. 2018; Rapp and Draper 2018). Coupled with the high density of Fe-rich ilmenite (Tronche et al. 2010) this late crystallization led to a gravitationally unstable mineral stratification in the lunar mantle (e.g., Taylor 1982; Snyder et al. 1992), prompting a large-scale mantle overturn (e.g., Hess and Parmentier 1995; de Vries et al. 2010; Zhang et al. 2013; Yu et al. 2019; Zhao et al. 2019; Maurice et al. 2020). Thermal effects associated with this overturn are believed to have triggered the formation and eruption of the lunar mare basalts that cover a significant part of the lunar near-side surface (e.g., Lucey et al. 2006) and could also have played a role in the generation of a lunar magnetic field (e.g., Stegman et al. 2003; Evans and Tikoo 2022).

Dedicated to Harry A.J. Oonk on the occasion of his eighty-fifth birthday.

✉ Michael H. G. Jacobs
Michael.Jacobs@TU-Clausthal.de

[1] Institute of Metallurgy, Clausthal University of Technology, Robert Koch Str. 42, 38678 Clausthal-Zellerfeld, Germany

[2] Department of Earth Sciences, Utrecht University, Princetonlaan 8a, 3584 CB Utrecht, The Netherlands

[3] Faculty of Science, Vrije Universiteit Amsterdam, Amsterdam, The Netherlands

[4] Bayerisches Geoinstitute, University of Bayreuth, Universitätsstraße 30, 95440 Bayreuth, Germany

Lunar evolution models require accurate knowledge of the physical and chemical properties of the geikielite–ilmenite solid solution as a function of composition, temperature and pressure. Recent studies have focused on obtaining equation of state data for both pure $FeTiO_3$ and natural ilmenite (Tronche et al. 2010 and references therein), and on rheological property measurements to constrain the flow behavior of ilmenite-bearing lunar rocks (Dygert et al. 2013, 2016, 2017; Tokle et al. 2021). To date, a full thermodynamic analysis of the geikielite–ilmenite solid solution has not been performed. In this study, we present a thermodynamic analysis of geikielite ($MgTiO_3$), ilmenite ($FeTiO_3$), and the geikielite–ilmenite solid solution. The analysis is based on a lattice vibrational method, from which we derive thermodynamic models for the end members and the solid solution phase formed from them.

Jacobs et al. (2019, 2017, 2007) demonstrated that models derived from lattice vibrational methods, such as the multiple-Einstein or Kieffer (1979) methods, result in accurate phase diagrams and thermodynamic properties free from unphysical behavior in the pressure–temperature regime of the Earth's (and the Moon's) interior. Besides, that, the formalism allows incorporating microscopic properties as model parameters, such as vibrational frequencies, Grüneisen, and anharmonicity parameters, which are derived from spectroscopic measurements or ab initio techniques. This characteristic, absent in conventional methods based on independent parameterizations of 1-bar properties (e.g., Saxena 1996; Holland and Powell 2011), puts extra constraints on a thermodynamic analysis, and that appears to be especially useful for discriminating between the quality of different experimental data sets, such as shown for, for instance, the heat capacity of the wadsleyite and ringwoodite forms of $Mg_2SiO_4$, the akimotoite and perovskite forms of $MgSiO_3$, and the coesite and stishovite forms of $SiO_2$ (Jacobs et al. 2019, 2017) This characteristic is also advantageous when experimental data are missing, such as is the case for bulk modulus for both geikielite and ilmenite. Because thermodynamic properties are interdependent due to their relation to microscopic and static energy properties, missing experimental data on the bulk modulus can be compensated by available microscopic data, such as frequencies of vibrational modes in $P$–$T$ space, in addition to thermodynamic data.

Both substances, geikielite and ilmenite, show phase transformations to different crystallographic structures when pressure is applied. Above 10 GPa, the perovskite form of $MgTiO_3$ and $FeTiO_3$, and a $CaTi_2O_4$-structured form of $Fe_2TiO_4$ have been found (e.g., Tschauner et al. 2020; Akaogi et al. 2017, 2019; Nishio-Hamane et al. 2012). However, the temperature–depth relation established by Maurice et al. (2020) and the $P$–$T$ phase diagrams of Akaogi et al. (2017, 2019) suggest that these high pressure phases do not occur in the interior of the Earth's Moon to a significant extent. According to these phase diagrams, the solid solution formed from $Mg_2TiO_4$ and $Fe_2TiO_4$ having a spinel structure may be important for application to the Earth's Moon. Although these phases may be relevant for lunar and terrestrial applications we have postponed thermodynamic analyses of them to a later stage of our database development and focus on thermodynamic properties of geikielite and ilmenite.

## Theoretical background

Jacobs et al. (2013) showed that the application of the multiple-Einstein formalism, in a thermodynamic analysis of data on thermophysical properties and phase diagrams, is mathematically and practically more convenient, than applying Kieffer's (1979) model directly. However, for substances, such as geikielite and ilmenite, for which no prediction of the Vibrational density of States (VDoS) is available by ab initio methods, two options are available to proceed. One option is to employ a minimum number of Einstein frequencies with different fractions and locations in the VDoS, such that thermodynamic properties are described accurately. The second option is to make use of available experimental spectroscopic data. Because the last option is less arbitrary, we have chosen to apply Kieffer's (1979) original model for performing the thermodynamic analysis in combination with an approximate VDoS determined from Raman and infrared spectroscopic data. Applying the thermodynamic analysis to all experimental data, including thermodynamic data, the location of the frequencies of the vibrational normal modes in the VDoS with their corresponding Grüneisen and anharmonicity parameters will be determined more accurately. For the sake of transparency, the resulting thermodynamic descriptions are converted to multiple-Einstein models. Just as in previous works of Jacobs et al. (2017, 2019), we have stored our results in a small database, which is together with open source computational software, freely available on website http://www.geo.uu.nl/~jacobs/Downloads. Because the application of Kieffer's method has been outlined in previous papers (e.g., Jacobs et al. 2005, 2007) we only briefly discuss the different formulations of the physical contributions in our method, and refer to the "online resource appendix" for further details.

The central equation for obtaining thermodynamic properties and shear modulus is a semi-empirical expression for the Helmholtz energy. Assuming that effects due to static lattice, vibrational, electronic and magnetic effects are additive we write this expression as

$$A(T,V) = U^{ref} + U^{static}(V) + A^{vib}(T,V) + A^{cf-el}(T) + A^{\lambda}(T) \quad (1)$$

The reference energy, $U^{ref}$ in Eq. (1), is a constant, and adjusted such that experimentally determined heats of formation of geikielite and ilmenite reported by Robie and Hemingway (1995) are represented. The static lattice energy, represented by the second term on the right-hand side of Eq. (1), is the result of changes in atomic attractive and repulsive energy contributions when the crystal volume is changed. This energy contribution is conveniently described by an equation of state for which we have chosen Vinet et al. (1987) or a third order Birch–Murnaghan (1952) expression. This contribution is a fictive property, because it does not include vibrational motions, such as present in a real crystal, but it can, in principle, be determined by athermal ab initio techniques. The third term in Eq. (1) is determined by vibrational motions. The VDoS has not been determined by ab initio methods for geikielite and ilmenite, and therefore, it is modelled using Kieffer's (1979) general expression, leading to the vibrational contribution to Helmholtz energy, given by Eq. (15) in the "online resource appendix".

The fourth term on the right-hand side of Eq. (1) takes into account crystal-field electronic effects in ilmenite. These effects were modelled in the same way as by Jacobs et al. (2019):

$$Z = \frac{1}{g_1}\sum_{i=1}^{m} g_i \exp\left(-\frac{\varepsilon_i}{kT}\right) \tag{2}$$

$$A^{cf-el} = -kT\ln Z - \frac{1}{2}\beta_{el}\frac{n_a}{N_A}\left(\frac{V}{V_0}\right)^{\gamma_{el}} T^2 \tag{3}$$

The Helmholtz energy contribution is given per atom Fe and for one site, $n_a$ is the number of Fe atoms in a molecular formula unit and $N_A$ represents Avogadro's number. The $m$ energy levels of one site are characterized by their energies, $\varepsilon_i$ and degeneracies $g_i$. The first energy level is assigned the ground state for with $\varepsilon_1 = 0$. Expressions for all thermodynamic properties derived from this Helmholtz energy contribution are detailed in Jacobs and de Jong (2009). Because experimental data for determining the effect of volume on the energies, $\varepsilon_i$, are absent we assume that they have constant values. Therefore, crystal field contributions affect only Helmholtz energy, entropy and heat capacity. The last term in Eq. (3) denotes a free-electron gas contribution and it is used in an alternative analysis for taking into account that isochoric heat capacities at high temperature exceed the Dulong–Petit limit.

The expression for the magnetic contribution to Helmholtz energy is based on Inden's (1981) model, and detailed in Jacobs et al. (2019). It is written as

$$A^{\lambda}(T) = n_a \cdot g(\tau) \cdot m_f \cdot RT\ln(1+\beta) \tag{4}$$

In Eq. (4), $n_a$ is the number of atoms in a molecular formula unit giving rise to a magnetic contribution ($n_a = 1$ for $FeTiO_3$), $g(\tau)$ a function depending on $\tau = T/T_c$ with $T_c$ the critical lambda temperature, $m_f$ is a correction factor, $R$ denotes the gas constant, $\beta$ the average magnetic moment per atom.

## Results

Geikielite and ilmenite belong to the ilmenite structure type with the rhombohedral space group $R\bar{3}$. The normal unit cell contains six molecules $MgTiO_3$ or $FeTiO_3$. Two molecules are present in the primitive cell. Therefore, 30 vibrational normal modes are present. Factor group analysis using the method of Fateley et al. (1971) results in the symmetry species of the three acoustic modes and 27 optic modes (Okada et al. 2008; Reynard and Guyot 1994):

$$\Gamma = 5A_g(R) + 5E_g(R) + A_u(1A) + 4A_u(IR) + E_u(1A) + 4E_u(IR) \tag{5}$$

In this representation, the $E_g$ and $E_u$ species are doubly degenerate, $R$ denotes Raman, $IR$ infrared and $1A$ acoustic modes. Hofmeister (1993) measured infrared reflectance spectra for natural ilmenite ($FeTiO_3$) and used her measurements, in combination with the factor group analysis, to construct an approximate vibrational density of states using Kieffer's (1979) method. Because geikielite is isostructural with ilmenite we used the same VDoS for both substances as a starting point in the optimization of all experimental data.

We performed the thermodynamic analysis of the two substances using the experimental data in Table 1. Table 1 shows that for geikielite vibrational frequencies of Raman modes were measured in large ranges of pressure and temperature, whereas for ilmenite these measurements are available at ambient conditions only. These measurements in $P$–$T$ space constrain Grüneisen parameters, their volume derivatives, and intrinsic anharmonicity parameters for the different vibrational modes. For that reason thermal expansivity, bulk modulus and heat capacity of geikielite are better constrained than for ilmenite. For ilmenite we have carried out two analyses, because Tronche et al. (2010) measured significantly larger volumes for their synthesized samples, relative to those of earlier investigations. For that reason, the $FeTiO_3$ data in Table 1 measured by Tronche et al. (2010) for synthetic samples are labeled by $FeTiO_3(2)$, whereas other data including the earlier investigations on synthetic samples are labeled by $FeTiO_3(1)$.

Because the amount of thermodynamic data is limited, we consider our calculated uncertainties in the model parameters as estimates. They are based on varying a specific model parameter such that the sum of squares changes outside its uncertainty range determined by the uncertainties in

**Table 1** Representation of experimental thermodynamic properties for $MgTiO_3$ (geikielite) and $FeTiO_3$ (ilmenite)

| Property | Max. relative deviation in % | Average relative deviation in % | *T*-range in K | *P*-range in GPa | References |
|---|---|---|---|---|---|
| $MgTiO_3$ (geikielite) | | | | | |
| Volume | 0.04 | 0.02 | 298–1163 | 0.0 | Tuval et al. (2020) |
| | 0.24 | 0.17 | 296–1578 | 0.0 | Henderson et al. (2009) |
| | 0.06 | 0.03 | 973–1573 | 0.0 | Zabicky et al (2009) |
| | 0.16 | 0.16 | 296 | 0.0 | Liferovich et al. (2006) |
| | 0.12 | 0.06 | 296 | 0.0–8.1 | Yamanaka et al. (2005) |
| | 0.05 | 0.05 | 296 | 0.0 | Wechsler et al. (1989) |
| $K_S$ | 0.04 | 0.04 | 293 | 0.0 | Liebermann (1976) |
| $V_P$ | 0.01 | 0.01 | 293 | 0.0 | Liebermann (1976) |
| $V_S$ | 0.01 | 0.01 | 293 | 0.0 | Liebermann (1976) |
| $G_{sh}$ | 0.60 | 0.60 | 293 | 0.0 | Liebermann (1976) |
| $\nu$ | 1.96 | 0.51 | 290 | 0.0–27.0 | Reynard and Guyot (1994) |
| | 2.04 | 0.57 | 290 | 0.0–30.0 | Okada et al (2008) |
| | 4.89 | 0.52 | 290–1000 | 0.0 | Reynard and Guyot (1994) |
| | 1.74 | 0.40 | 290–1000 | 0.0 | Okada et al. (2008) |
| $FeTiO_3$(1) (ilmenite, synthetic) | | | | | |
| Volume | 0.93 | 0.30 | 298–1273 | 0.0–16.0 | Tronche et al. (2010), natural |
| | 0.43 | 0.23 | 293 | 0.0–24.3 | Wu et al. (2009) |
| | 0.45 | 0.26 | 293 | 0.0–8.2 | Yamanaka et al. (2007) |
| | 0.12 | 0.05 | 297–1323 | 0.0 | Wechsler and Prewitt (1984) |
| | 0.11 | 0.05 | 297 | 0.0–4.6 | Wechsler and Prewitt (1984) |
| $FeTiO_3$(2) (ilmenite, synthesized by Tronche et al. 2010) | | | | | |
| Volume | 0.33 | 0.12 | 295–1273 | 0.0–16.0 | Tronche et al. (2010), synthetic |

$K_S$ denotes adiabatic bulk modulus, $V_P$ longitudinal and $V_S$ shear sound velocity, $\nu$ Raman frequencies, and $G_{sh}$ shear modulus. For $FeTiO_3$ Raman frequencies are available only at ambient conditions, described by optic continua in Tables 3, 4

**Table 2** Result of the thermodynamic analysis of $MgTiO_3$ geikielite

| Mode | Continuum | Fraction | $\nu$-range, $cm^{-1}$ | $\gamma_j$ | $a_j \times 10^5$ $K^{-1}$ | Peaks, $cm^{-1}$ |
|---|---|---|---|---|---|---|
| Acoustic | TA1 | 1/30 | 0–138 (10) | 3.26 (85) | 0.00 | |
| Acoustic | TA2 | 1/30 | 0–138 (10) | 3.26 (85) | 0.00 | |
| Acoustic | LA | 1/30 | 0–237 (7) | 1.39 (125) | 0.00 | |
| Eg ($\nu$5) | OC1 | 2/30 | 210 (16)–248 (16) | 1.142 (58) | − 5.53 (90) | 225 (Raman) |
| Ag ($\nu$5) | OC2 | 1/30 | 263 (6)–332 (6) | 1.037 (43) | − 1.74 (46) | 281 (Raman) |
| Eg ($\nu$4) | ,, | 2/30 | | | | 306 (Raman) |
| Ag ($\nu$4) | ,, | 1/30 | | | | 328 (Raman) |
| Eu (v4) | ,, | 2/30 | | | | 284 (IR) |
| Eg ($\nu$3) | OC3 | 2/30 | 371 (7)–501 (7) | 1.312 (33) | +0.76 (33) | 398 (Raman) |
| Eu (v2) | ,, | 2/30 | | | | 420–480 (IR) |
| Eg ($\nu$2) | ,, | 2/30 | | | | 501 (Raman) |
| Ag ($\nu$2) | OC4 | 1/30 | 491 (1)–493 (1) | 1.206 (19) | − 2.22 (88) | 487 (Raman) |
| Eg ($\nu$1) | OC5 | 2/30 | 542 (13)–729 (13) | 1.371 (28) | − 1.44 (25) | 641 (Raman) |
| Au (v1) | ,, | 1/30 | | | | 722 (IR) |
| Au (v2) | ,, | 1/30 | | | | 550 (IR) |
| Eu (v1) | ,, | 2/30 | | | | 620 (IR) |
| Ag ($\nu$1) | OC6 | 1/30 | 714.4 (9)–716.4 (9) | 0.891 (14) | +1.55 (6) | 716 (Raman) |
| Ag ($\nu$3) | OC7 | 1/30 | 264 (7)–425 (7) | 1.422 (40) | − 1.17 (42) | 354 (Raman) |
| Au (v4) | ,, | 1/30 | | | | 350 (IR) |
| Eu (v3) | ,, | 2/30 | | | | 377 (IR) |
| Au (v3) | ,, | 1/30 | | | | 420 (IR) |
| *Average* | | | | ***1.391 (34)*** | ***− 1.069 (154)*** | |
| Kieffer's model (Vinet's 1987 equation of state) | | | | | | |
| $V_0^{st}$, $cm^3$/mol | | $V_0$, $cm^3$/mol | $K_0^{st}$, GPa | $K_0'^{st}$ | | $U^{ref}$, kJ/mol |
| 30.459 (4) | | 30.734 (4) | 173.4 (21) | 3.40 (34) | | − 1622.7 (12) |
| Multiple-Einstein model (Birch–Murnaghan equation of state) | | | | | | |
| $V_0^{st}$, $cm^3$/mol | | $V_0$, $cm^3$/mol | $K_0^{st}$, GPa | $K_0'^{st}$ | | $U^{ref}$, kJ/mol |
| 30.451 (4) | | 30.743 (4) | 173.4 (21) | 3.36 (34) | | − 1622.7 (12) |
| | | $n_{s,0}$ | $G_0{}^{st}$, GPa | $G_0{}'^{st}$ | | |
| | | 1.27 (16) | 83.4 (24) | 1.32 (10) | | |

The Raman frequencies were taken from Reynard and Guyot (1994) and Okada et al. (2008). Infrared (IR) frequencies were taken from Baran and Botto (1978) and Hofmeister (1993). Frequencies in the last column are at ambient conditions. LA and TA denote longitudinal and transverse acoustic modes and OC optic continuum. All values in columns 4, 5 and 6 are at zero Kelvin and zero pressure. In Eq. (17) of "online resource appendix", all $m_j$ parameters were set to one, and all $\gamma_{j\infty}$ were set to zero. Parameters $G_0{}^{st}$, and $G_0{}'^{st}$ are the shear modulus and its pressure derivative of the static lattice and $n_{s,0}$ is a parameter needed for calculating the vibrational contribution to shear modulus

**Table 3** Result of the thermodynamic analysis for $FeTiO_3$ (ilmenite), denoted as $FeTiO_3(1)$ in the lower-right frame of Fig. 2

| Mode | Continuum | | Fraction | $\nu$-range, $cm^{-1}$ | $\gamma_j$ | $a_j \times 10^5$ $K^{-1}$ | Peaks, $cm^{-1}$ |
|---|---|---|---|---|---|---|---|
| Acoustic | TA1 | | 1/30 | 0–107.833 | 1.50 | 0.00 | |
| Acoustic | TA2 | | 1/30 | 0–107.833 | 1.50 | 0.00 | |
| Acoustic | LA | | 1/30 | 0–215.142 | 1.50 | 0.00 | |
| Eg ($\nu$5) | OC1 | | 2/30 | 157.14–182.91 | 1.142 (62) | − 6.5 (11) | 163 (R) |
| Ag ($\nu$5) | OC2 | | 1/30 | 162.42–375.00 | 1.037 (62) | − 6.5 (11) | 194 (R) |
| Ag ($\nu$3) | ,, | | 1/30 | | | | 329 (R) |
| Eg ($\nu$4) | ,, | | 2/30 | | | | 228 (R) |
| Ag ($\nu$4) | ,, | | 1/30 | | | | 251 (R) |
| Eu ($\nu$4) | ,, | | 2/30 | | | | 217–224 (IR) |
| Au ($\nu$4) | ,, | | 1/30 | | | | 262–320 (IR) |
| Eu ($\nu$3) | ,, | | 2/30 | | | | 282–355 (IR) |
| Au ($\nu$3) | ,, | | 1/30 | | | | 367–371 (IR) |
| Eg ($\nu$3) | OC3 | | 2/30 | 328.25–475.91 | 1.312 (62) | − 6.5 (11) | 368 (R) |
| Eu ($\nu$2) | ,, | | 2/30 | | | | 410–470 (IR) |
| Eg ($\nu$2) | ,, | | 2/30 | | | | Absent (R) |
| Ag ($\nu$2) | OC4 | | 1/30 | 455.00–457.00 | 1.206 (62) | − 6.5 (11) | 452 (R) |
| Eg ($\nu$1) | OC5 | | 2/30 | 496.91–760.00 | 1.371 (62) | − 6.5 (11) | 602 (R) |
| Au ($\nu$1) | ,, | | 1/30 | | | | 662–751 (IR) |
| Au ($\nu$2) | ,, | | 1/30 | | | | 602–504 (IR) |
| Eu ($\nu$1) | ,, | | 2/30 | | | | 506–756 (IR) |
| Ag ($\nu$1) | OC6 | | 1/30 | 679.00–681.00 | 0.891 (62) | − 6.5 (11) | 677 (R) |
| *Average* | | | | | ***1.213 (62)*** | ***− 6.5 (11)*** | |
| CFE | $E_1$ | $E_2$ | $E_3$ | $E_4$ | $E_5$ | | |
| | 0 | 86.7 (3) | 225.0 (13) | 10,000 | 10,000 | | |
| Inden's (1981) formalism for the lambda transition: $\beta = 4.00$, $m = 3$, $n = 5$, $T_C = 57.2$ K, $m_f = 0.682606$ (Eq. 4) | | | | | | | |
| Kieffer's model (Vinet's 1987 Equation of state) | | | | | | | |
| $V_0^{st}$, $cm^3$/mol | | | $V_0$, $cm^3$/mol | | $K_0^{st}$, GPa | $K_0^{'st}$ | $U^{ref}$, kJ/mol |
| 31.3838 (61) | | | 31.6152 (61) | | 172.6 (42) | 4.0(7) | − 1281.4 (25) |
| Multiple-Einstein model (Birch–Murnaghan equation of state) | | | | | | | |
| $V_0^{st}$, $cm^3$/mol | | | $V_0$, $cm^3$/mol | | $K_0^{st}$, GPa | $K_0^{'st}$ | $U^{ref}$, kJ/mol |
| 31.3828 (61) | | | 31.6136 (61) | | 172.8 (42) | 4.0 (7) | − 1281.2 (25) |
| | | | $n_{s,0}$ | | $G_0^{st}$, GPa | $G_0^{'st}$ | |
| | | | 0.88 (50) | | 89.2 (62) | 1.23 (40) | |

The infrared peak positions in the last column are taken from Hofmeister (1993) and the Raman peak positions from Wu et al. (2010). Frequencies in the last column are at ambient conditions. LA and TA denote longitudinal and transverse acoustic modes and OC optic continuum in Kieffer's (1979) model. All values in columns 4, 5 and 6 are at zero Kelvin and zero pressure. CFE denotes crystal field energies in $cm^{-1}$. Uncertainty in frequencies is less than 10 $cm^{-1}$. Mode Eg(v2) has not been experimentally verified. In an alternative analysis in which intrinsic anharmonicity is absent and use is made of Eq. (3) it follows that $\beta_{el} = (8 \pm 1) \times 10^{-3}$ J/K/mol and $\gamma_{el} = 0$. In Eq. (17) of "online resource appendix", all $m_j$ parameters were set to one, and all $\gamma_{j\infty}$ were set to zero. Parameters $G_0^{st}$, $G_0^{'st}$ and $n_{s,0}$ have the same meaning as in Table 2

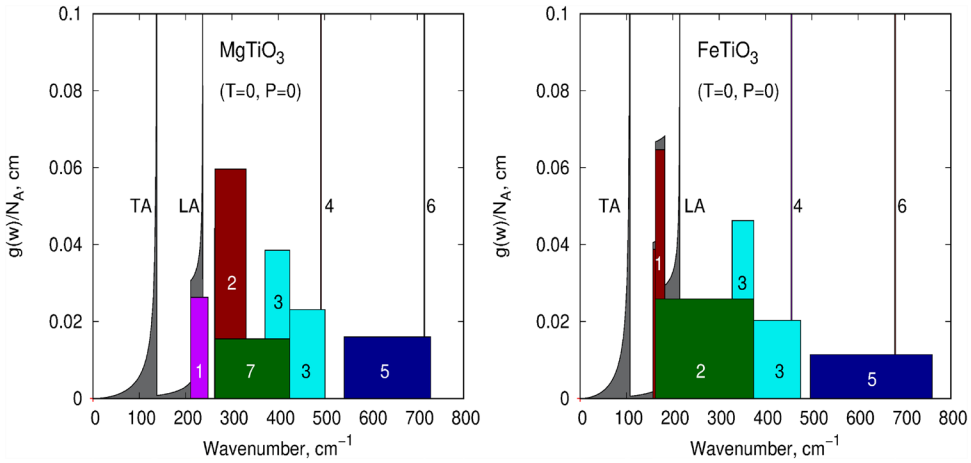


**Fig. 1** Kieffer models for the vibrational density of states of geikielite (left) and ilmenite (right). TA denotes transverse acoustic, LA longitudinal acoustic. Numbered boxes are optic continua consistent with the numbering in Tables 2, 3, 4. $N_A$ on the vertical axis denotes Avogadro's number. The surface underneath all continua, representing the total degree of vibrational freedom, is $3nN_A$ ($n=7$) for one mole of $MgTiO_3$ or $FeTiO_3$

experimental properties. Some trade-off between parameters in the Grüneisen expression, and intrinsic anharmonicity parameters given by, respectively, Eqs. (17) and (16) in the "online resource appendix", is present. The best representation of experimental data was achieved by setting parameters $m_j$ equal to one and $\gamma_{j\infty}$ equal to zero. From our thermodynamic analyses it appears that parameters dealing with the Grüneisen expression of the different vibrational optic modes of geikielite and ilmenite are similar. Therefore, we have used identical values for these parameters for both substances in the final result of Tables 2, 3.

The model parameters were obtained by a non-linear least squares technique described by Jacobs et al. (2017). The VDoS in terms of Kieffer's (1979) model resulting from the thermodynamic analysis of geikielite and ilmenite is plotted in Fig. 1. For the conversion of Kieffer's (1979) model to a multiple-Einstein model we employed 60 Einstein frequencies in the VDoS. Using the cloning process as discussed in Jacobs et al. (2017), the descriptions can be simplified to a smaller amount of Einstein frequencies in the VDoS.

The excess Gibbs energy and enthalpy of the solid solution formed from geikielite and ilmenite, (Mg, Fe)$TiO_3$, has been investigated by Linton et al. (1999) and Andersen et al. (1991). These investigations indicate that excess Gibbs energy can be described with a regular solution model with a Gibbs energy coefficient, $W_G$, between 0 and 4300 J/mol. The Gibbs energy of the solid solution, formed from the two end members, is expressed in the composition $x$ of $FeTiO_3$, the Gibbs energies of the end members $MgTiO_3$ and $FeTiO_3$, the ideal mixing term and the excess Gibbs energy as

$$\begin{aligned} G(P,T,x) =& (1-x)\,G^*_{MgTiO_3}(P,T) + x\,G^*_{FeTiO_3}(P,T) \\ &+ RT\,\{(1-x)\ln(1-x) + x\ln(x)\} \\ &+ W_G\,x(1-x) \end{aligned} \tag{6}$$

From the results discussed in the next two sections the Gibbs energies of the two end members in Eq. (6) can be derived as function of pressure and temperature. Subsequently, Eq. (6) allows the derivation of all thermodynamic properties of the solid solution in pressure–temperature–composition space, such as Gibbs energy, enthalpy, entropy, heat capacity, volume, thermal expansivity, bulk modulus and shear modulus.

## Discussion

In the sub-sections below we discuss our results obtained for $MgTiO_3$ (geikielite) and $FeTiO_3$ (ilmenite). Thermodynamic properties for the solid solutions in $P$–$T$ space follow directly from Eq. (6). We discuss these properties for conditions present in the Moon in "Solid solutions".

### $MgTiO_3$ (geikielite)

Our thermodynamic analysis of geikielite is constrained by Raman spectroscopic measurements of Reynard and Guyot (1994) and Okada et al. (2008), shown in Fig. 2. The eight infrared modes were constrained by the data of Baran and Botto (1978). Hofmeister (1993) determined the VDoS of ilmenite. We used her work as a basis to partition vibrational modes, having similar Grüneisen parameters, over optic continua in the VDoS. That resulted in ranges for the frequencies of the different vibrational modes, given by the optic continua OC1–OC7 in Table 2. For instance, modes grouped in OC2, such as Ag($\nu$4) and Ag($\nu$5), have similar frequencies and their Grüneisen parameters are about 1.04 at ambient conditions, as determined from the spectroscopic measurements. In the optimization process we used frequency data up to 20 GPa, because a study by Akaogi et al. (2019) indicates that $MgTiO_3$ decomposes into MgO and $TiO_2$ above this pressure. For that reason our calculated frequency–pressure curves deviate from the measurements above 20 GPa for a number of modes. This is visible in Fig. 2 for the

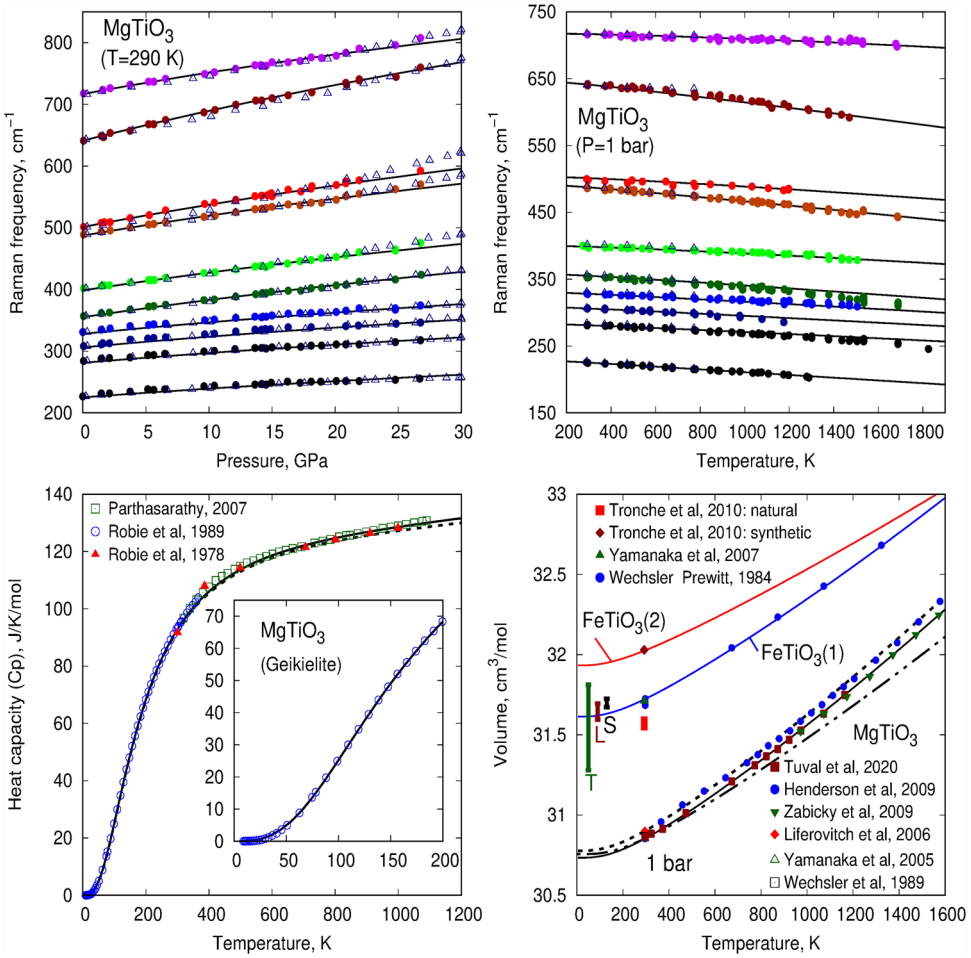


**Fig. 2** Upper-left and upper-right: Calculated and experimental frequencies of Raman modes at 290 K and 1 bar pressure. The solid circles represent the measurements of Reynard and Guyot (1994) and open triangles those of Okada et al. (2008). Lower-left: The solid curve represents heat capacity including anharmonicity in the lattice vibrations. The dashed curve represents a calculation in which the lattice vibrations behave quasi-harmonically. The small difference between the dashed and solid curves indicates that anharmonicity has an insignificant effect on heat capacity. Lower-right: The dot–dashed curve has been calculated with an average Grüneisen parameter for $MgTiO_3$ of 1.25. The dashed curve results from an optimization directed towards the data of Henderson et al. (2009), who synthesized a sample that likely contains an excess Ti, whereas the solid curve results from an optimization directed towards the data of Tuval et al. (2020) and Zabicky et al. (2009). The vertical bars labelled 'T', 'L' and 'S' are volumes of ilmenites measured at ambient conditions (the bars are offset from 300 K). The range of volumes reported in the literature for terrestrial samples is given by the vertical bar marked 'T'. That for Lunar samples is given by the bar marked 'L', and for synthetic samples by the bar marked 'S'. The curve labelled $FeTiO_3(2)$ belongs to a sample synthesized by Tronche et al. (2010), whereas the curve labelled $FeTiO_3(1)$ belongs to a synthetic sample with an ambient volume close to that for lunar samples

frequency–pressure curves of the modes $E_g(\nu 2)$, $A_g(\nu 2)$ and $E_g(\nu 3)$, which start at, respectively, 501, 487 and 398 $cm^{-1}$ and ambient pressure.

The final frequency location of the optic continua, after the optimization process, is mainly determined by the heat capacity data below room temperature, shown in the lower-left frame of Fig. 2. The spectroscopic data do not allow determining the lower and upper cutoff frequencies of the different optic continua in an strictly unambiguous way. For instance for OC2 a range between 250 and 340 $cm^{-1}$ would also be possible. In the optimization process that choice would affect the cutoff frequencies of the other continua, but the resulting thermodynamic properties are insignificantly affected. On the other hand the cutoff frequencies are not that arbitrary, because each continuum must contain all frequencies of the specified vibrational Raman and infrared modes in *P–T* space. The optimization of the frequency data in *P–T* space plotted in Fig. 2 results in the Grüneisen and anharmonicity parameters given in Table 2. The small difference between the solid and dashed heat capacity curves in Fig. 2 shows that the effect of anharmonicity has an insignificant effect on the heat capacity, and that also holds for other thermodynamic properties. The entropy at 298.15 K matches the experimental value $74.64 \pm 0.15$ J/K/mol, established

by Robie et al. (1989). Therefore, our description improves heat capacity and entropy established by Reynard and Guyot (1994), who found the value 73.5 J/K/mol using Kieffer's model with only two optic continua.

The infrared modes were investigated experimentally only at ambient conditions. Therefore, we assumed that infrared and Raman modes having similar frequencies, indicated in the last column of Table 2, have the same values for Grüneisen and anharmonicity parameters. This assumption needs some attention. The average Grüneisen parameter of the optic modes at zero pressure and zero temperature determined from our analysis is 1.25, consistent with the value between 1.1 and 1.3 determined by Reynard and Guyot (1994) but larger than the value 0.9 determined by Okada et al. (2008) at ambient conditions. The small value obtained by Okada et al. (2008) is only partially explained by their use of a smaller value for ambient isothermal bulk modulus, 161 GPa instead of 167 GPa resulting from our analysis. We refitted their data, when necessary with a quadratic expression, just as Reynard and Guyot (1994) did, and came to the conclusion that some of the modes such as Ag($\nu$4), Ag($\nu$5), Eg($\nu$1), Eg($\nu$3) and Eg($\nu$5) are in accordance with the measurements of Reynard and Guyot (1994), whereas other modes show significantly smaller Grüneisen parameters. The dot–dashed volume–temperature curve in Fig. 2 shows that volume expansion is sensitive to the average Grüneisen parameter. In particular, the curve shows that the average value for the Grüneisen parameter, between 0.9 and 1.3, derived from the optic modes established by Raman spectroscopic measurements of Okada et al. (2008) and Reynard and Guyot (1994) is too small to explain the volume expansion measured by Henderson (2009; Tuval et al. 2020) and Zabicky et al. 2009). These volume expansion data can only be explained by an average Grüneisen parameter of about 1.4. To establish this larger average value it may be assumed that a number of infrared modes are characterized by a large Grüneisen parameter or that the acoustic modes have larger Grüneisen parameters than the average. In Table 2, it has been assumed that larger Grüneisen parameters are present for the acoustic modes. Unfortunately no measurements of transverse and longitudinal sound velocities are available, other than at ambient conditions, to determine Grüneisen parameters for the three acoustic modes directly. The frequency location of the three acoustic modes in the VDoS

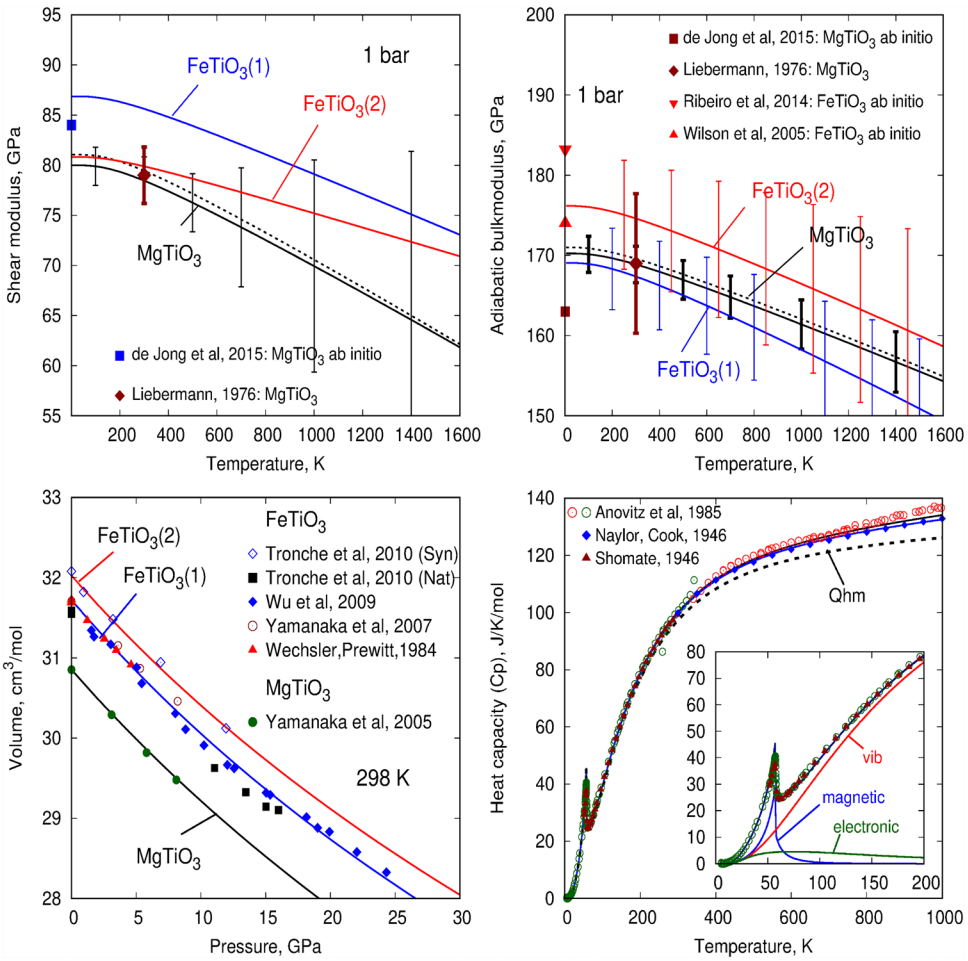


**Fig. 3** Upper-left, upper-right: Shear modulus and adiabatic bulk modulus at 1 bar. Only for $MgTiO_3$ an experimental datum is available. The solid curves for $MgTiO_3$ result from a description representing the *V–T* data of Tuval et al. (2020) and Zabicky et al. (2009) in Fig. 2, whereas the dashed curve results from that representing the *V–T* data of Henderson et al. (2009). Labels (1) and (2) have the same meaning as in the *V–T* plot of Fig. 2. The uncertainty bars result from propagation of uncertainties in the model parameters. Lower-left: volume–pressure curves at room temperature. 'Nat' denotes natural sample, and 'Syn' a synthetic sample. Lower-right: Heat capacity partitioned in physical effects for $FeTiO_3$. The upper solid curves represents heat capacity of $FeTiO_3$(1), whereas the lower solid curve that of $FeTiO_3$(2). The dashed curve has been calculated without intrinsic anharmonicity (quasi-harmonic model, Qhm)

is constrained by the sound wave velocity measurements of Liebermann (1976) at ambient conditions. Kieffer's (1979) model offers a method to determine the cutoff frequencies of these modes as shown in the "online resource appendix". Because the measurements were performed under ambient conditions, the accuracy of the shear modulus in *P–T* space is determined by the accuracy of the Grüneisen parameters of the acoustic modes, which in turn are constrained only by volume expansion/compression and heat capacity measurements. Figure 3 shows that our calculated value for shear modulus, 78.5 GPa, at ambient conditions, represents the experimental value established by Liebermann (1976). It is also consistent with the value of 84 GPa that is found in the data base of the Materials Project derived from first principles (de Jong et al. 2015, and website https://materialsproject.org/materials/mp-3771). No ab initio predictions or experimental results are available to constrain further the shear modulus as function of pressure and temperature. In an aside calculation we have incorporated larger Grüneisen parameters in the infrared modes. The easiest way to achieve this, without affecting heat capacity, is to partition the infrared modes over new optic continua OC2', OC3', OC5' and OC7' having the same cutoff frequencies as the optic continua OC2, OC3, OC5 and OC7, the latter four containing only the Raman modes. Assuming that Grüneisen parameters of the acoustic modes are 1.25, and that the Grüneisen parameters of the infrared modes are all identical, results in a value of 1.80 for them after optimization of the data in Table 1. This description results in an insignificantly different representation of heat capacity, bulk modulus, *V–T* data, and shear modulus. Whether the acoustic modes or the infrared modes have larger Grüneisen parameters could in principle be determined, apart from sound velocity measurements and direct measurements of the infrared modes, from thermal expansivity experiments below room temperature. Because the acoustic modes have smaller frequencies than the infrared modes, they are excited first at low temperatures. Therefore, larger Grüneisen parameters of the acoustic modes would result in a steeper behavior of thermal expansivity with temperature relative to the case of larger Grüneisen parameters in the infrared modes, about 34% larger at 100 K. However, such measurements are presently absent for geikielite.

Although no measurements of bulk modulus are available at temperatures above room temperature, Kieffer's (1979) method allows predicting it, because thermodynamic properties are interdependent due to their relation to microscopic properties. In this method bulk modulus is the sum of static and vibrational contributions, $K^{static}(V) + K^{vib}(T,V)$. The lower-left frame of Fig. 3 shows that static bulk modulus, which depends only on volume, is determined by the compression experiments of Yamanaka et al. (2005), characterized by a volume change of -4.4% at their highest measured pressure of 8.1 GPa relative to ambient conditions. In addition, it is constrained by the volume expansion data plotted in Fig. 2, resulting in a volume change of + 4.5% at the highest temperature of 1573 K relative to ambient conditions. The static bulk modulus is entirely determined by its value, $K_0^{static}$, and its pressure derivative, $K_0'^{static}$, at zero pressure. Bulk modulus is also determined by its vibrational contribution, which depends on vibrational frequencies and Grüneisen parameters. This contribution is much smaller compared to the static contribution, about 1.2 GPa at ambient conditions, and 0.4 GPa at 1000 K and 1 bar pressure. Bulk modulus is, therefore, mainly constrained by volume expansion and compression and to a lesser extent by the behavior of vibrational frequencies in *P–T* space. That bulk modulus is related to thermal expansivity is also illustrated by the thermodynamic identity:

$$\alpha K = \left(\frac{\partial P}{\partial T}\right)_V = \left(\frac{\partial P^{vib}}{\partial T}\right)_V \tag{7}$$

In Eq. (7), the last step is obtained, because only the thermal pressure denoted by $P^{vib}$ is temperature dependent, and it is derived from the vibrational contribution to Helmholtz energy, Eq. (15) in "online resource appendix". Because vibrational frequencies in *P–T* space depend on volume their description requires the equation of state. Expression (7) indicates that model parameters describing the bulk modulus are constrained by *V–P–T* measurements and microscopic properties, which in turn are also constrained by the heat capacity. Therefore, relative to methods employing parameterizations for 1 bar thermodynamic properties, no extra independent parameterization for 1-bar bulk modulus is required in our method.

The thin uncertainty bars plotted in Fig. 3 were obtained by the propagation of uncertainties in the model parameters into bulk modulus. They are smaller than the uncertainty in the bulk modulus measured by Liebermann (1976), because the model parameters are additionally constrained by the volume, heat capacity and vibrational frequency data. Figure 3 shows that because the shear modulus depends on the behavior of the acoustic frequencies in *P–T* space, for which no measurements are available, its uncertainty increases rapidly with temperature. Therefore, extra measurements are required to constrain this property more accurately.

Related to the findings above, some remarks on sample characterization of geikielite are appropriate here. Figure 2 shows that we have directed our optimization towards the *V–T* data of Tuval et al. (2020) and Zabicky et al. (2009). The *V–T* data sets of Henderson et al. (2009) and those of Tuval et al. (2020) are based on different samples. The data set of Henderson et al. (2009) is based on a mixture of small amounts of $TiO_2$ (rutile) and $MgTiO_3$, and a large amount of $MgTi_2O_5$ (karrooite), whereas that of Tuval et al. (2020) is

based on a mixture of 95 wt% $MgTiO_3$ and 5 wt% $Mg_2TiO_4$ (qandilite). According to Shindo (1980) and Wechsler and Navrotsky (1984), $MgTiO_3$ is a non-stoichiometric compound, which is able to dissolve a small excess quantity of Ti, but not Mg. Tuval et al. (2020) showed experimentally and with the help of the phase diagram of MgO–$TiO_2$ published by Shindo (1980), that their sample contains $MgTiO_3$ near the stoichiometric composition, whereas the sample of Henderson et al. (2009) most likely contains an excess of Ti, which explains the difference between the available *V*–*T* data sets. The *V*–*T* data set of Zabicky et al. (2009) is consistent with that of Tuval et al. (2020), because their sample is also a mixture of $MgTiO_3$ and $Mg_2TiO_4$. The dashed curves in Fig. 3 show that the different *V*–*T* descriptions plotted in Fig. 2 have an insignificant effect on the bulk- and the shear modulus. Concerning the spectroscopic measurements, Reynard and Guyot (1994) did not mention how geikielite was synthesized, nor was a characterization to stoichiometry carried out. Okada et al. (2008) synthesized geikielite by a solid state reaction of MgO and $TiO_2$ and also did not detail the stoichiometry of the obtained sample. It is possible that differences in Grüneisen parameters for a number of modes obtained by Reynard and Guyot (1994) and Okada et al. (2008) are related to the amount of Ti in the samples. The effect of stoichiometry on measured Raman frequencies is, therefore, uncertain.

In the multiple-Einstein model we have made the simplification that no dispersion is present in the Grüneisen, mode-*q* and anharmonicity parameters. For these parameters at zero temperature and zero pressure, we took the average values, obtained using the parameters weighed to the fractions in the corresponding acoustic and optic continua in Kieffer's model. It appears that thermodynamic properties above room temperature are insignificantly affected. The largest difference takes place at high temperature. For instance at 1600 K and 1 bar, adiabatic bulk modulus differs by only 0.4%, heat capacity by 0.08%, volume by 0.01% and thermal expansivity by 0.6%. Below room temperature the largest difference is present in thermal expansivity, 10% at 150 K. Other properties are insignificantly different, such as bulk modulus, 0.07%, and volume, 0.03%. The effect of dispersion in the microscopic parameters on thermodynamic properties is, therefore, insignificant.

## $FeTiO_3$ (ilmenite)

The vertical bar labeled 'T' in the *V*–*T* plot of Fig. 2 shows that large differences for ambient volume of the terrestrial (natural) ilmenites are available in the literature. The differences are likely due to the presence of variable amounts of elements such as Al, Cr, Mg, Mn, Si and V in the investigated samples, although the precise effect on volume due to each element is not known. In addition, it has been found (Thorpe et al. 1977; Bayer et al. 1972; Raymond and Wenk 1971; Haggerty et al. 1970; Stewart et al. 1970) that natural samples, contain variable amounts of $Fe^{3+}$, having the tendency of reducing the *c*-axis length of the unit cell. Differences in volume are significantly smaller for lunar ilmenites labeled 'L' in Fig. 2. Samples of these materials, which are also not exactly pure $FeTiO_3$, were found to be free of $Fe^{3+}$ and contain an excess amount of Ti, probably in the form of $Ti^{3+}$ (Bayer et al. 1972), which has the tendency to increase the *c*-axis length of the unit cell. Volumes of lunar samples are comparable in value with those of synthetic samples of $FeTiO_3$, labeled 'S' in Fig. 2. Relative to these synthetic samples, Tronche et al. (2010) synthesized $FeTiO_3$ with a significant 1% larger ambient volume, labeled $FeTiO_3$(2) in Fig. 2. The *c*-axis is about 0.15% longer than that of other synthetic samples, whereas the *a*-axis is about 0.4% longer. According to Tronche et al. (2010) several explanations for their larger volume relative to earlier investigations are possible. The first one is that samples synthesized in earlier investigations might contain an amount of $Fe^{3+}$ that went unnoticed in the experiments and due to the fact that no true $fO_2$ buffer was applied. Another reason could be that the starting composition of the sample was not clearly documented, such as in the experiments of Yamanaka et al. (2007) plotted in Figs. 2, 3, or that the oxidation state of samples was not monitored and controlled during the heating and compression experiments. A problem that has not been addressed by the different investigations, next to the explanations mentioned above, is that the solid solubility range around the $FeTiO_3$ stoichiometric composition indicated in the phase diagram of FeO–$TiO_2$ reported by MacChesney and Muan (1961), could be quite large, although the precise solid solubility range has not been established experimentally. Therefore, some of the investigations that we used in Figs. 2, 3 may include samples that suffered from a deviation from the $FeTiO_3$ stoichiometric composition. For instance Tronche et al. (2010) report a Ti/Fe ratio of 1.08–1.12 for their synthetic sample indicating some deviation from stoichiometry. Wechsler and Prewitt (1984) and Yamanaka et al. (2007) did not report such a ratio, and therefore, it is unclear if their synthetic samples were purely stoichiometric. Only for lunar and terrestrial natural samples Ti/Fe ratios are available. The lunar sample that Thorpe et al. (1977) used contained a smaller Ti/Fe ratio of 1.03, whereas Raymond and Wenk (1971) found 1.04 for a different lunar sample. A mathematical relationship between volume and/or *a*-axis and *c*-axis lengths and Ti/Fe ratio has not been established yet, and therefore, the difference in volume measured by Tronche et al. (2010) relative to other synthetic samples cannot be attributed unambiguously to the deviation from stoichiometry. Because synthetic $FeTiO_3$ samples are available with significantly different volumes we performed two separate thermodynamic analyses for them.

Our approach in the thermodynamic analysis of $FeTiO_3$ is similar to that for $MgTiO_3$, with the difference that frequencies of the Raman and infrared modes are available only at ambient conditions, measured by Wu et al. (2010) and Hofmeister (1993), respectively. For that reason, Grüneisen parameters and their volume derivatives for $FeTiO_3$ cannot be derived from experiments, and therefore, we assumed that they are identical to those of $MgTiO_3$. To match the *V–T* behavior at 1 bar pressure, shown in Fig. 2 for $FeTiO_3$(1), modes Ag(v3), Au(v4), Eu(v3) and Au(v3) in OC7 must have Grüneisen parameters significantly smaller, 1.04 instead of 1.4 for geikielite. Therefore, we joined these modes together with those already present in OC2. The number of optic continua for $FeTiO_3$ is thus six instead of seven, which simplifies the VDoS. Just as for geikielite, the location of the cutoff frequencies of the vibrational modes is mainly determined by the heat capacity below room temperature. According to Anovitz et al. (1985), $FeTiO_3$ is characterized by a paramagnetic–antiferromagnetic transition at 57.2 K. To describe this lambda transition, we employed Inden's (1981) model in the same way as Jacobs et al. (2019) did for $FeSiO_3$ (orthoferrosilite). Two types of electronic contributions are present. The first one is a crystal-field splitting of the *d*-energy levels of the iron atoms, because they are octahedrally surrounded by oxygen atoms. The other electronic contribution is due to a metal to metal charge transfer (MMCT) between Fe and Ti atoms (e.g., Taran 2019). Because energy levels of these two effects were not experimentally resolved we modeled them by a simple tentative crystal-field contribution with three $t_{2g}$ and two $e_g$ energy levels as indicated in Table 3. The different contributions to heat capacity are shown in the inset plot of Fig. 3. In the optimization process, the crystal field contribution has the effect, that it prevents the cutoff frequencies of the optic continua for shifting to too low frequencies, such that they do not include the experimental Raman and infrared frequencies. Our calculated entropy at 298.15 K and 1 bar pressure is 108.2 J/K/mol, in agreement with the value of 108.9 J/K/mol experimented by Anovitz et al. (1985) on a synthetic sample, although no uncertainty in their value was reported. Shomate et al. (1946) reports a smaller value of $105.8 \pm 1.25$, because their heat capacity is about 0.7% smaller at 150 K, and because their measurements do not cover the region between 0 and 50 K.

The dashed heat capacity curve in Fig. 3 shows that calculations performed in the quasi-harmonic approximation result in a significant underestimation of this property above room temperature. The difference can be caused by intrinsic anharmonicity or an electronic effect or a combination of them. Jacobs et al. (2019) showed for $FeSiO_3$ compounds that modeling high-temperature heat capacity with either an electronic contribution, such as by employing the second term on the right-hand side of Eq. (3), or intrinsic anharmonicity does not lead to significantly different results, and that applies to $FeTiO_3$ too. Table 3 shows for ilmenite that the average value for intrinsic anharmonicity is about 6.5 times larger than that of geikielite, when the high-temperature heat capacity is described with intrinsic anharmonicity only, similar to findings for $FeSiO_3$. For synthetic samples with ambient volumes comparable with those obtained from the Moon, labeled $FeTiO_3$(1) in Figs. 2, 3, our description for high-temperature heat capacity is in between the experimental data of Anovitz et al. (1985) and those of Naylor and Cook (1946).

We have determined the average Grüneisen parameter of $FeTiO_3$(1) by the *V–T* curve measured by Wechsler and Prewitt (1984) at 1 bar pressure, depicted in Fig. 2. To obtain this average Grüneisen parameter, we optimized those of the acoustic modes under the assumption that the values for the transverse and longitudinal modes are equal, resulting in a value of 1.5 for them. Values for the individual Grüneisen parameters for $FeTiO_3$ are much less robust relative to those for $MgTiO_3$. Only the average value of them leads to a robust description of the volume expansion. In our optimization we

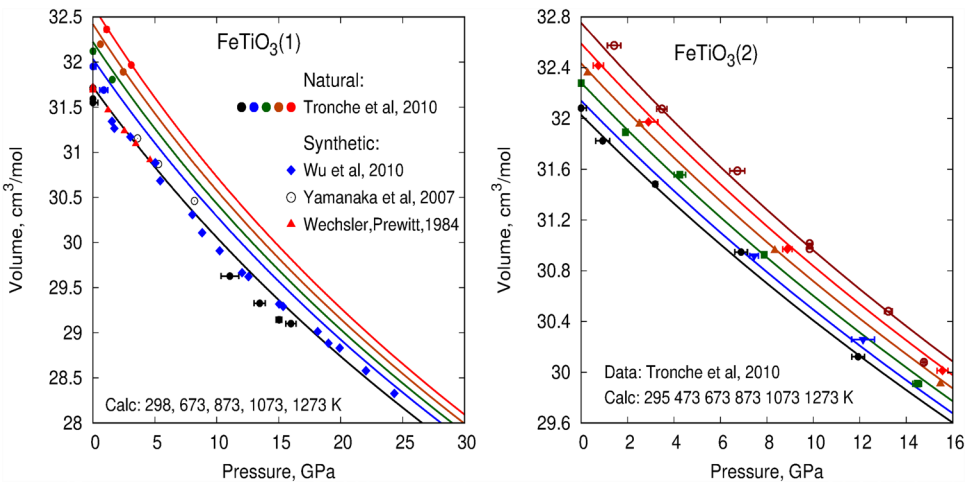


**Fig. 4** Left: Calculated isotherms compared to experimental data. The data of Tronche et al. (2010) were measured for a natural sample from the Jagersfontein mine, south Africa. The other data were obtained for synthetic samples. (1) has the same meaning as the *V–T* plot of Fig. 2. Right: Calculated isotherms for a sample synthesized by Tronche et al. (2010) and labeled $FeTiO_3$(2) in Fig. 2

**Table 4** Result of the thermodynamic analysis for $FeTiO_3$ (ilmenite), denoted as $FeTiO_3(2)$ in the lower-right frame of Fig. 2

| Mode | Continuum | | Fraction | $\nu$-range, $cm^{-1}$ | $\gamma_j$ | $a_j \times 10^5$ $K^{-1}$ | Peaks |
|---|---|---|---|---|---|---|---|
| Acoustic | TA1 | | 1/30 | 0–107.83 | 1.50 | 0.00 | |
| Acoustic | TA2 | | 1/30 | 0–107.83 | 1.50 | 0.00 | |
| Acoustic | LA | | 1/30 | 0–215.14 | 1.50 | 0.00 | |
| Eg ($\nu$5) | OC1 | | 2/30 | 157.14–182.91 | 0.929 (66) | − 6.5 (11) | 163 (R) |
| Ag ($\nu$5) | OC2 | | 1/30 | 162.42–375.00 | 1.037 (66) | − 6.5 (11) | 194 (R) |
| Ag ($\nu$3) | ,, | | 1/30 | | | | 329 (R) |
| Eg ($\nu$4) | ,, | | 2/30 | | | | 228 (R) |
| Ag ($\nu$4) | ,, | | 1/30 | | | | 251 (R) |
| Eu ($\nu$4) | ,, | | 2/30 | | | | 217–224 (IR) |
| Au ($\nu$4) | ,, | | 1/30 | | | | 262–320 (IR) |
| Eu ($\nu$3) | ,, | | 2/30 | | | | 282–355 (IR) |
| Au ($\nu$3) | ,, | | 1/30 | | | | 367–371 (IR) |
| Eg ($\nu$3) | OC3 | | 2/30 | 328.25–475.91 | 0.873 (66) | − 6.5 (11) | 368 (R) |
| Eu ($\nu$2) | ,, | | 2/30 | | | | 410–470 (IR) |
| Eg ($\nu$2) | ,, | | 2/30 | | | | Absent (R) |
| Ag ($\nu$2) | OC4 | | 1/30 | 455.00–457.00 | 1.206 (66) | − 6.5 (11) | 452 (R) |
| Eg ($\nu$1) | OC5 | | 2/30 | 496.91–760.00 | 1.001 (66) | − 6.5 (11) | 602 (R) |
| Au ($\nu$1) | ,, | | 1/30 | | | | 662–751 (IR) |
| Au ($\nu$2) | ,, | | 1/30 | | | | 602–504 (IR) |
| Eu ($\nu$1) | ,, | | 2/30 | | | | 506–756 (IR) |
| Ag ($\nu$1) | OC6 | | 1/30 | 679.00–681.00 | 0.891 (66) | − 6.5 (11) | 677 (R) |
| *Average* | | | | | ***1.037 (66)*** | ***− 6.5 (11)*** | |
| CFE | $E_1$ | $E_2$ | $E_3$ | $E_4$ | $E_5$ | | |
| | 0 | 86.7 (3) | 225.0 (13) | 10,000 | 10,000 | | |
| Inden's (1981) formalism for the lambda transition: $\beta = 4.00$, $m = 3$, $n = 5$, $T_C = 57.2$ K, $m_f = 0.682606$ (Eq. 4) | | | | | | | |
| Kieffer's (1979) model with Vinet et al. (1987) | | | | | | | |
| $V_0^{st}$, $cm^3$/mol | | | $V_0$, $cm^3$/mol | | $K_0^{st}$, GPa | $K_0^{'st}$ | $U^{ref}$ |
| 31.7496 (315) | | | 31.9332 (315) | | 179.3 (57) | 4.0 (14) | − 1281.3 (25) |
| Multiple-Einstein model (Birch–Murnaghan equation of state) | | | | | | | |
| $V_0^{st}$, $cm^3$/mol | | | $V_0$, $cm^3$/mol | | $K_0^{st}$, GPa | $K_0^{'st}$ | $U^{ref}$ |
| 31.7488 (315) | | | 31.9388 (315) | | 179.0 (57) | 4.0 (14) | − 1281.1(25) |
| | | | $n_{s,0}$ | | $G_0^{st}$, GPa | $G_0^{'st}$ | |
| | | | 0.67 (50) | | 82.6 (80) | 1.05(40) | |

The infrared peak positions in the last column are taken from Hofmeister (1993) and the Raman peak positions from Wu et al. (2010). Frequencies in the last column are at ambient conditions. LA and TA denote longitudinal and transverse acoustic modes and OC optic continuum in Kieffer's (1979) model. All values in columns 4, 5 and 6 are at zero Kelvin and zero pressure. CFE denotes crystal field energies in $cm^{-1}$. Uncertainty in frequencies is about 10 $cm^{-1}$. Mode Eg(v2) has not been experimentally verified. In an alternative analysis in which intrinsic anharmonicity is absent and use is made of Eq. (3) it follows that $\beta_{el} = (8 \pm 1) \times 10^{-3}$ J/K/mol and $\gamma_{el} = 0$. In Eq. (17) of "online resource appendix", all $m_j$ parameters were set to one, and all $\gamma_{j\infty}$ were set to zero. Parameters $G_0^{st}$, $G_0^{'st}$ and $n_{s,0}$ have the same meaning as in Table 2

did not include the *V–P–T* data for a natural sample measured by Tronche et al. (2010), plotted in the left frame of Fig. 4. Because the calculated isotherms apply to synthetic samples, Fig. 4 gives an indication that this natural sample (from Jagersfontein mine, South Africa) shows a different volume expansion relative to synthetical ones. Although the number of measurements and the pressure range above room temperature is small, it is visible that the difference between our calculations and the data points becomes smaller as temperature increases. This indicates that thermal expansivity of this natural sample is larger than that for a synthetic ilmenite sample, and comparable with that for geikielite. This might be the effect of $Fe^{3+}$, or the presence of other elements, such as a large amount of Mg in this sample, about 7.8 wt%.

Just as for $MgTiO_3$, no experimental data for bulk modulus are available in *P–T* space, and we predicted its behavior with Kieffer's method. Because Grüneisen parameters are not as well constrained as for $MgTiO_3$, the uncertainty in bulk modulus is larger. Our predicted value of $169 \pm 4$ GPa at zero temperature and zero pressure is in fair agreement with the value 174 GPa predicted by Wilson et al. (2005) using ab initio, but it deviates from the ab initio value of Ribeiro and Lázaro (2014), 183.24 GPa. The volume–pressure data set for $FeTiO_3$(1) given in Figs. 3, 4 measured by Wu et al. (2009) contributes to the accuracy of our determined bulk modulus. Their data do not show a phase transformation from the ilmenite to the perovskite structure, although the *P–T* phase diagram found by Ming et al. (2006) and Akaogi et al. (2017) indicates that above 16 GPa the perovskite structure should be stable. Therefore, taking into account the *V–P* data above 16 GPa does not affect our determined value for bulk modulus to a significant extent. The shear modulus curve, plotted in the upper-left frame of Fig. 3, is not robust but tentative, because no measurements are available for this property, not even at ambient conditions. We followed the assumption by Hofmeister (1993) that, because ambient bulk sound velocity of ilmenite and hematite are similar, this will also hold for ambient longitudinal and transverse sound velocities. Because this introduces an unknown systematic uncertainty, no uncertainty bars are plotted for this property in Fig. 3.

For the sample synthesized by Tronche et al. (2010), characterized by the large volume labeled $FeTiO_3$(2) in Fig. 2, our calculation of high-temperature heat capacity prefers the data of Naylor and Cook (1946) depicted in Fig. 3, due to a smaller thermal expansivity. Our predicted value of isothermal bulk modulus at zero temperature and zero pressure is $176 \pm 6$ GPa, which is in between the values predicted by Wilson et al. (2005) and Ribeiro and Lázaro (2014). The average Grüneisen parameter has been determined using the *V–P–T* data of Tronche et al. (2010), shown in the right-hand frame of Fig. 4. These data require a smaller average Grüneisen parameter than for $FeTiO_3$(1), 1.04 instead of 1.21. Because it was not possible to adjust the Grüneisen parameters of only the acoustic modes, keeping those of the optic modes identical to those of $FeTiO_3$(1), we changed some of the optic modes. The resulting solution reported in Table 4 is, however, not unique and other values for Grüneisen parameters are possible. This increases the uncertainty in predicted bulk and shear modulus plotted in the upper two frames of Fig. 3 relative to that for $FeTiO_3$(1).

In the multiple-Einstein model we have made the same simplification as for $MgTiO_3$, that no dispersion is present in the Grüneisen, mode-*q* and anharmonicity parameters. Also in the case of $FeTiO_3$, it appears that thermodynamic properties are insignificantly affected, and therefore, the effect of dispersion in the microscopic parameters on thermodynamic properties is insignificant.

## Solid solution

Ilmenite bearing cumulates (IBC) contain iron rich solid solutions of $MgTiO_3$ (geikielite) and $FeTiO_3$ (ilmenite). The solid solution ilmenite, having the same name as its end member $FeTiO_3$, is denoted by the formula $(Mg_{1-x},Fe_x)TiO_3$, indicating that Mg and Fe atoms mix via a substitutional mechanism. The ilmenite solid solution originates from a late stage fractional crystallization process of a lunar magma ocean. Petrological models (e.g., Snyder et al. 1992; Lin et al. 2017a, b) indicate that the iron content, *x*, in the solid solution increases significantly with progressing solidification from the melt. Tokle et al. (2021) argued that the magnesium composition of the ilmenite solid solution might increase by a process of re-equilibration of late and early cumulates, through the mechanism of dissolution and re-precipitation during melt–rock reactions. In such scenario, the solidification process may have resulted in a chemically differentiated layering of ilmenite solid solutions on a small scale within the IBC layer, due to the non-uniform iron content. Besides buoyancy effects the iron content also affects the viscosity of ilmenite in the IBC material (Tokle et al. 2021). These two effects have a significant impact on triggering and development of the lunar mantle overturn. In mantle dynamic scenarios the dense IBC layer sinks, during the overturn, through the less dense olivine and pyroxene material to the bottom of the mantle, producing a relatively stable layering, impacting the thermal evolution of mantle and core (de Vries et al. 2010; Zhao et al. 2019). The fraction of the IBC retained at shallower level depends critically on the detailed structure of the initial layering (Zhao et al. 2019). Upwellings from a dense layer of IBC deposited at the core mantle boundary during overturn are possibly related to titanium basalts observed at the lunar surface (Tokle et al. 2021; Zhang et al. 2017, 2013; Zhong et al. 2000). Compositional variation within the ilmenite solid solution would then be reflected in the composition of

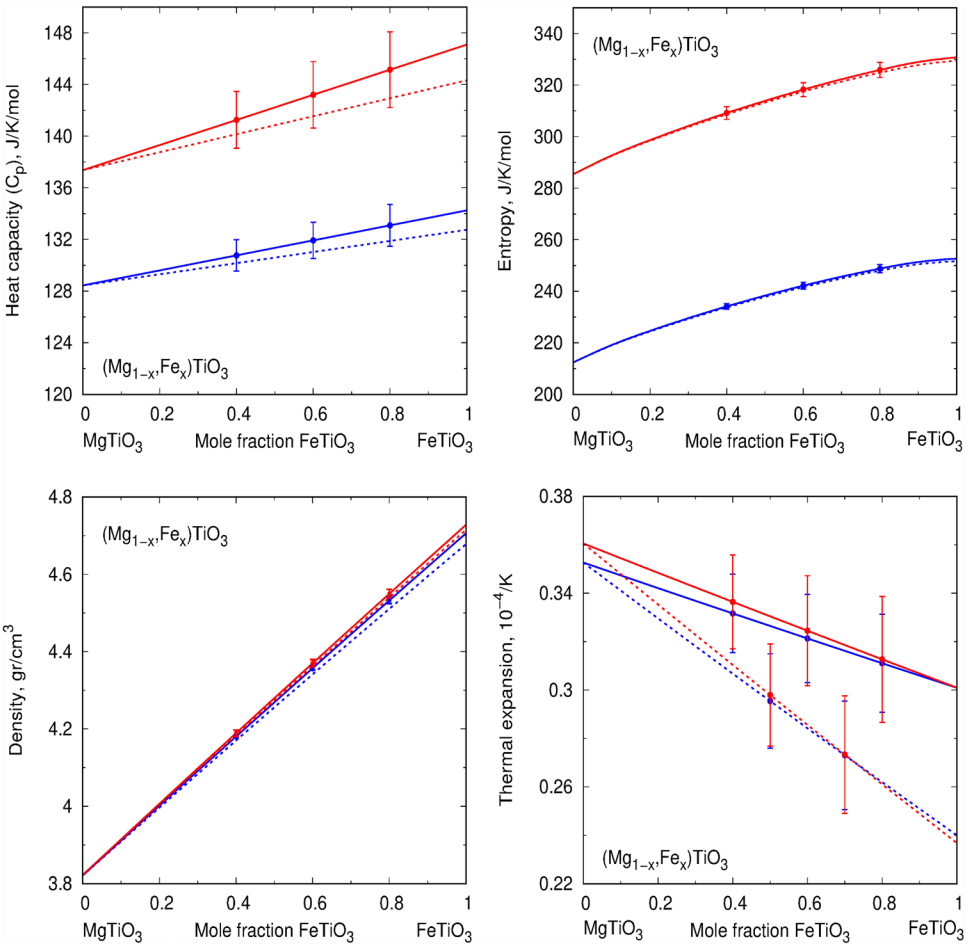


**Fig. 5** Thermodynamic properties calculated for mixtures in the system $MgTiO_3$–$FeTiO_3$(1) are plotted as solid curves and those for mixtures in the system $MgTiO_3$–$FeTiO_3$(2) as dashed curves. The red curves were calculated at 1800 K and 5 GPa, and the blue ones at 1000 K and 0.5 GPa, simulating conditions of the CMB and upper mantle in the moon, respectively. Uncertainty bars in calculated properties are based on uncertainties in the established model parameters

the Ti-basalts. Such secondary upwellings from the deeper mantle will also be sensitive to density gradients resulting from chemical variation in the IBC layer, produced by the fractional solidification process.

These conjectures can be investigated in numerical modeling experiments with a mantle convection model that incorporates material properties for a compressible medium and with a thermodynamic self-consistent representation of solid solutions. Such convection models could then be used to obtain estimates of the composition of basaltic lavas produced in secondary upwellings, especially in combination with an improved melting phase diagram for the IBC material.

As a first step towards such a convection model, thermo physical properties required in convection models for the Moon mantle were evaluated for ilmenite solid solutions in the relevant part of the *P*–*T* domain. Figure 5 illustrates the effect of variable iron content on the physical properties of ilmenite solid solutions. In particular the effect of composition on density is expected to be significant for the mantle dynamics described above. Figure 5 demonstrates that uncertainties in the thermodynamic properties, make it difficult to distinguish between ilmenites for which the iron end member has the thermodynamic description of $FeTiO_3$(1) or that of $FeTiO_3$(2), except for thermal expansivity. Ilmenites having the $FeTiO_3$(2) description for the iron end member show a much stronger effect of composition on thermal expansivity than those having the $FeTiO_3$(1) description. The four plots also show that the effect of temperature and pressure, in the Moon mantle *P*–*T* range, on density and thermal expansivity is small relative to the effect of composition, in contrast to these effects on heat capacity and entropy. Figure 1 on "Online resource appendix" shows that the effect of pressure, temperature and composition on bulk and shear modulus is insignificant. These properties may be treated as constants to within their estimated uncertainty.

## Conclusions

Conclusions drawn from our study are given below.

1. Kieffer's (1979) method, in combination with Raman and infrared spectroscopic data and the estimated VDoS determined by Hofmeister (1993), is suitable for

deriving robust thermodynamic properties for $MgTiO_3$ (geikielite) and $FeTiO_3$ (ilmenite).

2. Relative to methods relying on independent parameterizations of 1-bar thermodynamic properties, Kieffer's method has the advantage of predicting bulk modulus for these two substances in *P–T* space.
3. Intrinsic anharmonicity has an insignificant effect on the heat capacity of geikielite. However, for ilmenite heat capacity is significantly affected by either a strong high-temperature electronic effect or intrinsic anharmonicity, or both.
4. The average Grüneisen parameter of geikielite derived from Raman spectroscopic measurements is too small to explain its 1-bar volume–temperature behavior. Therefore, either the acoustic modes or some infrared modes are characterized by Grüneisen parameters larger than the average value. Based on the available data, our analysis is unable to indicate which vibrational modes must have larger Grüneisen parameters relative to this average. However, aside calculations indicate that thermodynamic properties, including our predicted bulk and shear modulus, are insignificantly affected if either the acoustic modes or infrared modes are responsible for the larger Grüneisen parameters. The average Grüneisen parameter at zero temperature and zero pressure is largest for geikielite, 1.39(3), and smallest for an ilmenite sample synthesized by Tronche et al. (2010), 1.04(7). Other synthetic ilmenite samples have an average Grüneisen parameter of 1.21(6).
5. Combining the measurements of Tronche et al. (2010) and our calculations on synthetic samples suggest that the ilmenite sample obtained from Jagersfontein, South Africa has a thermal expansivity comparable with that of geikielite.
6. The non-stoichiometry of the geikielite sample, used by Henderson et al. (2009), affects volume significantly, but it has no significant effect on the bulk modulus, shear modulus and heat capacity.
7. Our predicted shear modulus of geikielite represents an experimental datum point at ambient conditions, but it is not very reliable at higher temperatures and pressures. Our predicted shear modulus for ilmenite in *P–T* space is less reliable relative to geikielite, because the value at ambient conditions is based on the assumption that longitudinal and transverse sound velocities are similar to those of hematite. Constraining shear modulus better requires sound velocity measurements for both geikielite and ilmenite in *P–T* space. In turn this would enable improved assessments of future seismic measurements of the Moon's interior.
8. For ilmenite it is possible that the large volume measured by Tronche et al. (2010) is due to the effect of non-stoichiometry. Although the Ti/Fe ratio of two lunar samples gave us a reason for making this statement, we cannot attribute the large volume due to this ratio unambiguously, because no experimental relation between volume and Ti/Fe ratio has been established. Therefore, it is also possible, as Tronche et al. (2010) suggest, that in earlier work ilmenite samples were not synthesized under a true $fO_2$ buffer.
9. We showed with multiple-Einstein models that dispersion in the mode Grüneisen and anharmonicity parameters has an insignificant effect on thermodynamic properties. The static equation of state parameters of the Vinet equation of state that we used for our Kieffer models are insignificantly different from the Birch–Murnaghan equation of state parameters that we used for our multiple-Einstein models.
10. The thermodynamic descriptions of geikielite and ilmenite allow predicting thermodynamic properties and shear modulus of the solid solution formed from them in pressure–temperature–composition space.

Results obtained in this paper are, together with open source computational software, freely available on website http://www.geo.uu.nl/~jacobs/Downloads.

**Supplementary Information** The online version contains supplementary material available at https://doi.org/10.1007/s00269-022-01195-5.

**Acknowledgements** MHG Jacobs gratefully acknowledges financial support by the German Research Foundation (DFG) under grant no. JA 1985/1-2. Collaboration between A. van den Berg and M. Jacobs has been supported through The Netherlands Research Center for Integrated Solid Earth Science (ISES) project ME-2.7. W. van Westrenen would like to thank the Dutch Research Council for funding through a Vici grant. We express our gratitude to two anonymous reviewers for their constructive and insightful suggestions which improved the quality of the manuscript significantly.

## References

Akaogi M, Abe K, Yusa H, Ishii T, Tajima T, Kojitani H, Mori D, Inaguma Y (2017) High-pressure high-temperature phase relations in $FeTiO_3$ up to 35 GPa and 1600 °C. Phys Chem Miner 44:63–74

Akaogi M, Tajima T, Okano M, Kojitani H (2019) High-pressure and high-temperature phase relations in $Fe_2TiO_4$ and $Mg_2TiO_4$ with implications for titanomagnetite inclusions in superdeep diamonds. Minerals 9(614):2–12

Andersen DJ, Bishop FC, Lindsley DH (1991) Internally consistent solution models for Fe-Mg-Mn-Ti oxides: Fe-Mg-Ti oxides and olivine. Am Miner 76:427–444

Anovitz LM, Treiman AH, Essene EJ, Hemingway BS, Westrum EF Jr, Wall VJ, Burriel R, Bohlen SR (1985) The heat-capacity of ilmenite and phase equilibria in the system Fe-Ti-O. Geochim Cosmochim Acta 49:2037–2040

Baran EJ, Botto IL (1978) Die IR-spektren einiger doppeloxiden mit ilmenit-struktur. Z Anorg Allg Chem 444:282–245

Bayer G, Felsche J, Schulz RP (1972) X-ray study and mössbauer spectroscopy on lunar ilmenites (Apollo 11). Earth Planet Sci Lett 16:273–274

Birch F (1952) Elasticity and constitution of the earth's interior. J Geophys Res 57:227–286
Charlier B, Grove TL, Namur O, Holz F (2018) Crystallization of the lunar magma ocean and the primordial mantle-crust differentiation of the moon. Geochim Cosmochim Acta 234:50–69
de Jong M, Chen W, Angsten T, Jain A, Notestine R, Gamst A, Sluiter M, Ande CK, van der Zwaag S, Plate JJ, Toher C, Curtarolo S, Ceder G, Persson KA, Asta M (2015) Charting the complete elastic properties of inorganic crystalline compounds. Scientific Data 2:150009
de Vries J, van den Berg AP, van Westrenen W (2010) Formation and evolution of a lunar core from ilmenite-rich magma ocean cumulates. Earth Planet Sci Lett 292(1–2):139–147
Dygert N, Liang Y, Hess P (2013) The importance of melt $TiO_2$ in affecting major and trace element partitioning between Fe-Ti oxides and lunar picritic glass melts. Geochim Cosmochim Acta 106:134–151
Dygert N, Hirth G, Liang Y (2016) A flow law for ilmenite in dislocation creep: implications for lunar cumulate mantle overturn. Geophys Res Lett 43:532–540
Dygert N, Lin J-F, Marshall EW, Kono Y, Gardner JE (2017) A low viscosity lunar magma ocean forms a stratified anorthitic flotation crust with mafic poor and rich units. Geophys Res Lett 44:11282–11291
Evans AJ, Tikoo SM (2022) An episodic high-intensity lunar core dynamo. Nat Astron. https://doi.org/10.1038/s41550-021-01574-y
Fateley WG, McDevitt NT, Bently FF (1971) Infrared and Raman selection rules for lattice vibrations: the correlation method. Appl Spectrosc 25:155–174
Haggerty SE, Boyd FR, Bell PM, Finger LW, Bryan WB (1970) Iron titanium oxides and olivine from 10020 and 10071. Science 167:613–615
Henderson CMB, Knight KS, Lennie AR (2009) Temperature dependence of rutile ($TiO_2$) and geikielite ($MgTiO_3$) structures determined using neutron powder diffraction. Open Mineral J 3:1–11
Hess PC, Parmentier EM (1995) A model for the thermal and chemical evolution of the moon's interior: implication for the onset of mare volcanism. Earth Planet Sci Lett 134:501–514
Hofmeister AM (1993) IR reflectance spectra of natural ilmenite: comparison with isostructural compounds and calculation of thermodynamic properties. Eur J Miner 5:281–295
Holland TJB, Powell R (2011) An improved and extended internally consistent thermodynamic dataset for phases of petrological interest, involving a new equation of state for solids. J Metamorph Geol 29:333–383
Inden G (1981) The role of magnetism in the calculation of phase diagrams. Physica 103B:82–100
Jacobs MHG, de Jong BHWS (2005) Quantum-thermodynamic treatment of intrinsic anharmonicity; Wallace's theorem revisited. Phys Chem Miner 32:614–626
Jacobs MHG, de Jong BHWS (2007) Placing constraints on phase equilibria and thermophysical properties in the system MgO-$SiO_2$ by a thermodynamically consistent vibrational method. Geochim Cosmochim Acta 71:3630–3655
Jacobs MHG, de Jong BHWS (2009) Thermodynamic mixing properties of olivine derived from lattice vibrations. Phys Chem Miner 36:365–389
Jacobs MHG, Schmid-Fetzer R, van den Berg AP (2013) An alternative use of Kieffer's lattice dynamics model using vibrational density of states for constructing thermodynamic databases. Phys Chem Miner 40:207–227
Jacobs MHG, Schmid-Fetzer R, van den Berg AP (2017) Phase diagrams, thermodynamic properties and sound velocities derived from a multiple Einstein method using vibrational densities of states: an application to MgO-$SiO_2$. Phys Chem Miner 44:43–62
Jacobs MHG, Schmid-Fetzer R, van den Berg AP (2019) Thermophysical properties and phase diagrams in the system MgO-$SiO_2$-FeO at upper mantle and transition zone conditions derived from a multiple-Einstein method. Phys Chem Miner 46:513–534
Kieffer SW (1979) Thermodynamics and lattice vibrations of minerals: 3. Lattice dynamics and an approximation for minerals with application to simple substances and framework silicates. Rev Geophys Space Phys 17:35–59
Liebermann RC (1976) Elasticity of ilmenites. Phys Earth Planet Inter 12:P5–P10
Liferovich RP, Mitchell RH (2006) The pyrophanite-geikielite solid solution series: crystal structures of the $Mg_{1-x}Zn_xTiO_3$ series ($0<x<0.7$). Can Miner 44:1099–1107
Lin Y, Tronche EJ, Steenstra ES, van Westrenen W (2017a) Evidence for an early wet moon from experimental crystallization of the lunar magma ocean. Nat Geosci 10:14–18
Lin Y, Tronche EJ, Steenstra ES, van Westrenen W (2017b) Experimental constraints on the solidification of a nominally dry lunar magma ocean. Earth Planet Sci Lett 471:104–116
Lin Y, Hui H, Xia X, Shang S, van Westrenen W (2020) Experimental constraints on the solidification of a hydrous lunar magma ocean. Meteorit Planet Sci 55(1):207–230
Linton JA, Fei Y, Navrotsky A (1999) The $MgTiO_3$-$FeTiO_3$ join at high pressure and temperature. Am Miner 84:1595–1603
Lock SJ, Stewart ST, Petaev M, Leinhardt Z, Mace MT, Jacobsen SB, Ćuk M (2018) The origin of the moon within a terrestrial synestia. J Geophys Res Planets 123:910–951
Lucey P, Korotev RL, Gillis JJ, Taylor LA, Lawrence D, Campbell BA, Elphic R, Feldman B, Hood LL, Hunten D, Mendillo M, Noble S, Papike JJ, Reedy RC, Lawson S, Prettyman T, Gasnault O, Maurice S (2006) Understanding the lunar surface and space-moon interactions. Rev Mineral Geochem 60:83–219
MacChesney JB, Muan A (1961) Phase equilibria at liquidus temperatures in the system iron oxide—titanium oxide at low oxigen pressures. Am Miner 16:572–582
Maurice M, Tosi N, Schwinger S, Breuer D, Kleine T (2020) A long-lived magma ocean on a young Moon. Sci Adv 6(28):1–10
Ming LC, Kim YH, Uchida T, Wang Y, Rivers M (2006) In situ X-ray diffraction study of phase transitions of $FeTiO_3$ at high pressures and temperatures using a large-volume press and synchrotron radiation. Am Miner 91:120–126
Nakajima M, Stevenson DJ (2018) Inefficient volatile loss from the moon-forming disk: reconciling the giant impact hypothesis and a wet moon. Earth Planet Sci Lett 487:117–126
Naylor BF, Cook OA (1946) High-temperature heat contents of the metatitanates of calcium, iron and magnesium. J Amer Chem Soc 68:1003–1005
Nishio-Hamane D, Zhang M, Yagi T, Ma Y (2012) High-pressure and high-temperature phase transitions in $FeTiO_3$ and a new dense $FeTi_3O_7$ structure. Am Miner 97:568–572
Okada T, Narita T, Nagai T, Yamanaka T (2008) Comparative Raman spectroscopy study on ilmenite-type $MgSiO_3$ (akimotoite), $MgGeO_3$, and $MgTiO_3$ (geikielite) at high temperatures and high pressures. Am Miner 93:39–47
Parthasarathy G (2007) High-temperature electrical resistivity and heat capacity studies on nano-crystalline geikielite. Mater Lett 61:3208–3210
Rapp JF, Draper DS (2018) Fractional crystallization of the lunar magma ocean: updating the dominant paradigm. Meteorit Planet Sci 53(7):1432–1455
Raymond KN, Wenk HR (1971) Lunar ilmenite (refinement of the crystal structure). Contrib Miner Pertrol 30:135–140
Reynard B, Guyot B (1994) High-temperature properties of geikielite ($MgTiO_3$-ilmenite) from high-temperature high-pressure Raman spectroscopy–some implications for $MgSiO_3$-ilmenite. Phys Chem Miner 21:441–450

Ribeiro RAP, de Lázaro SR (2014) Structural, electronic and elastic properties of $FeBO_3$ (B=Ti, Sn, Si, Zr) ilmenite: a density functional theory study. RSC Adv 4:59839–59846

Robie RA, Hemingway BS, Fisher JR (1978) Thermodynamic properties of minerals and related substances at 298.15 K and 1 bar and at higher temperatures. US Geol Surv Bull 456:266–267

Robie RA, Haselton HT Jr, Hemingway BS (1989) Heat capacities and entropies at 298.15 K of $MgTiO_3$ (geikielite), ZnO (zincite), and $ZnCO_3$ (smithsonite). J Chem Thermodyn 21:743–749

Robie RA, Hemingway BS (1995) Thermodynamic properties of minerals and related substances at 298.15 K and 1 bar (105 Pascals) pressure and at higher temperatures. US Geol Surv Bull No. https://doi.org/10.3133/b2131

Saxena SK (1996) Earth mineralogical model: gibbs free energy minimization computation in the system MgO-FeO-$SiO_2$. Geochim Cosmochim Acta 60(1):2379–2395

Shindo I (1980) Determination of the phase diagram by the slow cooling float zone method: the system MgO-$TiO_2$. J Cryst Growth 50:839–851

Shomate CH (1946) Heat capacities at low temperatures of the metatitanates of iron, calcium and magnesium. J Amer Chem Soc 68:964–966

Snyder GA, Taylor LA, Neal CR (1992) A chemical model for generating the sources of mare basalts: combined equilibrium and fractional crystallization of the lunar magmasphere. Geochimica Cosmochimica Acta 56:3809–3823

Steenstra ES, Rai N, Knibbe JS, Lin YH, van Westrenen W (2016) New geochemical models of the core formation in the moon from metal-silicate partitioning of 15 siderophile elements. Earth Planet Sci Lett 441:1–9

Steenstra ES, Berndt J, Klemme S, Fei Y, van Westrenen W (2020) A possible high-temperature origin of the moon and its geochemical consequences. Earth Planet Sci Lett 538:116222

Stegman DR, Jellinek A, Zatman S, Baumgardner JR, Richards MA (2003) An early lunar core dynamo driven by thermochemical mantle convection. Nature 421:143–146

Stewart DB, Appleman DE, Huebner JS, Clark JR (1970) Crystallography of some lunar plagioclase. Science 167:634–638

Taran MN (2019) Electronic intervalence $Fe^{2+}+Ti^{4+}\rightarrow Fe^{3+}+Ti^{3+}$ charge-transfer transition in ilmenite. Phys Chem Miner 46:839–843

Taylor SR (1982) Planetary science: a lunar perspective. Lunar and Planetary Institute, Houston, p 481

Thorpe AN, Minkin JA, Senftle FE, Alexander C, Briggs C, Evans HT Jr, Nord GL Jr (1977) Cell dimensions and antiferromagnetism of lunar and terrestrial ilmenite single crystals. J Phys Chem Solids 38:115–123

Tokle L, Hirth G, Raterron P, Liang Y, Dygert N (2021) The effect of pressure and Mg-contents on ilmenite rheology: Implications for lunar cumulate mantle overturn. J Geophys Res Planets. https://doi.org/10.1029/2020JE006494

Tronche EJ, van Kan PM, de Vries J, Wang Y, Sanehira T, Li J, Chen B, Gao L, Klemme S, McCammon CA, van Westrenen W (2010) Thermal equation of state of $FeTiO_3$ ilmenite based on in situ X-ray diffraction at high pressure and temperatures. Am Miner 95:1708–1716

Tschauner O, Ma C, Newville MG, Lanzirotti A (2020) Structure analysis of natural wangdaodeite-$LiNbO_3$-type $FeTiO_3$. Minerals 10(1072):1–12

Tuval T, Rosen BA, Zabicky J, Kimmel G, Dilman H, Shneck RZ (2020) Thermal expansion of $MgTiO_3$ made by sol-gel technique at temperature range 25–890 °C. Curr Comput-Aided Drug Des 10(887):2–11

Vinet P, Ferrante J, Rose JH, Smith JR (1987) Compressibility of solids. J Geophys Res 92:9319–9325

Wechsler BA, Navrotsky A (1984) Thermodynamics and structure chemistry of compounds in the system MgO-$TiO_2$. J Solid State Chem 55:165–180

Wechsler BA, Prewitt CT (1984) Crystal structure of ilmenite ($FeTiO_3$) at high temperature and at high pressure. Am Miner 69:176–185

Wechsler BA, von Dreele RB (1989) Structure refinements of $Mg_2TiO_4$, $MgTiO_3$ and $MgTi_2O_5$ by time-of-flight neutron powder diffraction. Acta Cryst B45:542–549

Wilson NC, Muscat J, Mkhonto D, Ngoepe PE, Harrison NM (2005) Structure and properties of ilmenite from first principles. Phys Rev B 71(075202):1–9

Wu X, Steinle-Neumann G, Narygina O, Kantor I, McCammon C, Pascarelli S, Aquilanti G, Dubrovinsky L (2009) Iron oxidation state of $FeTiO_3$ under high pressure. Phys Rev B 79(094106):1–7

Wu X, Qin S, Dubrovinsky L (2010) Structural characterization of the $FeTiO_3$-$MgTiO_3$ solid solution. J Solid State Chem 183:2483–2489

Yamanaka T, Komatsu Y, Sugahara M, Nagai T (2005) Structure change of $MgSiO_3$, $MgGeO_3$, and $MgTiO_3$ ilmenites under compression. Am Miner 90:1301–1307

Yamanaka T, Komatsu Y, Nomori H (2007) Electron density distribution of $FeTiO_3$ ilmenite under high pressure analyzed by MEM using single crystal diffraction intensities. Phys Chem Miner 34:307–318

Yu S, Tosi N, Schwinger S, Maurice M, Breuer D, Xiao L (2019) Overturn of ilmenite-bearing cumulates in a rheologically weak lunar mantle. J Geophys Res Planets 124:418–436

Zabicky J, Kimmel G, Goncharov E, Guirado E (2009) Magnesium titanate phases from xerogels by hot stage X-ray powder diffraction. Z Krist Suppl 30:347–352

Zhang N, Parmentier EM, Liang YA (2013) A 3-D numerical study of the thermal evolution of the moon after cumulate mantle overturn: the importance of rheology and core solidification. J Geophys Res Planets 118:1789–1804

Zhang N, Dygert N, Liang Y, Parmentier EM (2017) The effect of ilmenite viscosity on the dynamics and evolution of an overturned lunar cumulate mantle. J Geophys Res Lett 44:6543–6552

Zhao Y, de Vries J, van den Berg AP, Jacobs MHG, van Westrenen W (2019) The participation of ilmenite-bearing cumulates in lunar mantle overturn. Earth Planet Sci Lett 511:1–11

Zhong S, Parmentier EM, Zuber MT (2000) A dynamic origin for the global asymmetry of lunar mare basalts. Earth Planet Sci Lett 177:131–140